Formation and annihilation of bulk recombination-active defects induced by muon irradiation of crystalline silicon

Anup Yadav,[1] Tim Niewelt,[1,2,3] Sophie L. Pain,[1] Nicholas E. Grant,[1] James S. Lord,[4] Koji Yokoyama,[4] and John D. Murphy[1,a]

AFFILIATIONS

[1]School of Engineering, University of Warwick, Coventry CV4 7AL, United Kingdom
[2]Fraunhofer Institute for Solar Energy Systems ISE, Heidenhofstraße 2, 79110 Freiburg, Germany
[3]Institute for Sustainable Systems Engineering, University of Freiburg, Emmy-Noether-Straße 2, 79110 Freiburg, Germany
[4]STFC Rutherford Appleton Laboratory, ISIS Neutron and Muon Source, Didcot OX11 0QX, United Kingdom

[a]Author to whom correspondence should be addressed: john.d.murphy@warwick.ac.uk

ABSTRACT

Muons are part of natural cosmic radiation but can also be generated at spallation sources for material science and particle physics applications. Recently, pulsed muons have been used to characterize the density of free charge carriers in semiconductors and their recombination lifetime. Muon beam irradiation can also result in the formation of dilute levels of crystal defects in silicon. These crystal defects are only detected in high carrier lifetime silicon samples that are highly sensitive to defects due to their long recombination lifetimes. This work investigates the characteristics of these defects in terms of their formation, recombination activity, and deactivation. Charge carrier lifetime assessments and photoluminescence imaging have great sensitivity to measure the generated defects in high-quality silicon samples exposed to ∼4 MeV (anti)muons and their recombination activity despite the extremely low concentration. The defects reduce the effective charge carrier lifetime of both *p*- and *n*-type silicon and appear to be more detrimental to *n*-type silicon. Defects are created by transmission of muons through the wafer, and there are indications that slowed or implanted muons may create additional defects. In a post-exposure isochronal annealing study, we observe that annealing at temperatures of up to 450 °C does not by itself fully deactivate the defects. A recovery of charge carrier lifetime was observed when the annealing was combined with Al_2O_3 surface passivation, probably due to passivation of bulk defects from hydrogen from the dielectric film.

I. INTRODUCTION

Muon spin spectroscopy (*μ*SR) is a pivotal technique for probing the magnetic and electronic properties of materials.[1] It involves the measurement of spatial distribution of positrons emitted upon muon decay using detectors positioned around the sample. In our previous studies, it has been demonstrated that photoexcited *μ*SR (photo-*μ*SR) can be used for depth-dependent charge carrier lifetime measurements in silicon wafers and completed solar cells.[2–5] The photo-*μ*SR technique involves exciting charge carriers with a pulsed laser light and implantation of pulses of "surface" muons (i.e., positive muons, *μ*+, featuring kinetic energy around 4 MeV). This process yields a muon spin asymmetry time spectrum, providing crucial information about the material characteristics. In case of photo-*μ*SR, the muon spin asymmetry can be used to probe free carrier densities in a semiconductor sample and their recombination decay after optical charge carrier generation. After their implantation in the semiconductors, the fully spin-polarized positive muons capture electrons to form muonium atoms. Muonium functions analogous to a hydrogen isotope,[6] for instance, in chemical reactions or acting as an impurity in semiconductor materials. Muonium presence in

semiconductors (e.g., Si and Ge) can give information about the material's electronic conditions.[7-9]

Initially, it was believed that recombination centers created by muons would have a minimal impact on the bulk carrier lifetime of silicon as the concentration was lower than other defect-related recombination centers present in the silicon bulk, meaning the muon beam can typically be regarded as an inert probe. However, this assumption is not true for high-quality silicon material used in silicon photovoltaics, which has a lifetime in the millisecond range. In our most recent study, we found that muon implantation introduces defects in the silicon crystal resulting in charge carrier lifetime reduction measured both *in situ* with photo-μSR and *ex situ* using photoconductance techniques.[5] The beam damage was likely only observed due to the extreme sensitivity of carrier lifetime in silicon even to small crystal damage, with recombination center densities of order $10^{10}\,cm^{-3}$ later measured by deep-level transient spectroscopy (DLTS). In this paper, we revisit the defects created in muon-irradiated silicon. We investigate *p*- and *n*-type substrates with high initial material quality and suppressed surface recombination via atomic layer deposition (ALD) of aluminum oxide layers. We aim to understand the defects created due to the implantation of muons, through a variety of post-exposure characterization methods and processing approaches.

II. EXPERIMENTAL METHODS

A. Sample preparation

Samples were fabricated from $725\,\mu m$ thick Czochralski-grown silicon (100) wafers. The wafers were either 200 mm diameter phosphorus-doped *n*-type wafers with a resistivity of 500–1200 Ω cm or 200 mm diameter boron-doped *p*-type Czochralski-grown silicon (100) wafers with a resistivity of 1000 or 2000 Ω cm. The wafers featured one chemically polished side and one non-polished side, which does not have a strong impact on the effectiveness of the surface passivation used.[10] For ease of handling, samples of $5 \times 5\,cm^2$ were cleaved from the wafers, and these were individually passivated with Al_2O_3 to reduce surface recombination. Prior to passivation, the samples underwent a wet chemical cleaning process optimized by Grant *et al.*[11] This involved sequential immersion in heated solutions at 80 °C for 10 min each. The cleaning steps included standard clean 1 [SC1: de-ionized water, ammonium hydroxide (30%), and hydrogen peroxide (30%) in a 5:1:1 ratio], tetramethylammonium hydroxide (TMAH) solution (25%), and standard clean 2 [SC2: de-ionized water, hydrochloric acid (HCl, 37%), and hydrogen peroxide (30%) in a 5:1:1 ratio]. This cleaning procedure is hereafter referred to as SC1-TMAH-SC2. A de-ionized water rinse and a 60 s dip in hydrofluoric acid (HF, 1%) preceded each cleaning and etching step. After the cleaning process, the samples were immersed in a 1% HF/1% HCl solution for 5 min. Note that we did not rinse the samples in water between the HF/HCl dip and subsequent layer deposition. Surface passivation layers were formed using ALD in a Veeco Fiji G2 system featuring an external load lock. Al_2O_3 was deposited on both sides of the samples at 200 °C using a plasma O_2 source and a trimethylaluminum precursor for 250 cycles to give films of ~25 nm thickness. Samples were subsequently annealed in air at 450–460 °C to "activate" the passivation, with this passivation scheme demonstrated

to give a surface recombination velocity of $<1\,cm\,s^{-1}$ in our laboratory.[12]

B. Muon implantation

The experiment uses anti-muons (or "positive muons") that will be addressed simply as muons throughout this article for the sake of brevity. Implantation of 3.8 MeV muons was carried out in the EMU spectrometer at ISIS Neutron and Muon Source at the STFC Rutherford Appleton Laboratory.[13] The samples were kept at 305 K using a closed cycle refrigerator (CCR) setup. A rectangular aperture in the muon beam with slit size corresponding to a width of 14 mm was usually used to restrict muon implantation to a part of the sample, enabling direct comparison of exposed and unexposed regions on the same silicon sample, although in one case a 48 mm aperture was used. The experimental setup for sample mounting is illustrated in Fig. 1. Samples were mounted onto a metal sample holder. Silicone vacuum grease was used to ensure good thermal contact. Different configurations of aluminum degrader foils were placed in front of the samples, as illustrated in Fig. 1(a). Figure 1(b) shows the sample covered with degraders from the muon-exposed side mounted on the CCR. The degrader foils enabled us to achieve different implantation depths and levels of dissipated energy per muon, with details shown in Table II.

Two different experiments were conducted, denoted as experiments I and II. In experiment I, samples underwent two distinct muon exposure conditions. Samples P2, N2, and N3 were subjected to muon implantation at fixed depths of 366, 366, and 609 μm, respectively, for approximately 12 h. The number of muon implantation events was estimated from the count rates of the scintillator detectors of the EMU spectrometer usually used for μSR integrated over exposure time. For sample P2, this amounted to approximately 1476 millions of events (MEv), while for N2 and N3, it was approximately 1430 MEv, as stated in Table I. Sample N1 and N6 were exposed to muons at three different implantation depths labelled as Pos 1, Pos 2, and Pos 3. Each exposure lasted approximately 50 min, resulting in a cumulative exposure of 2.5 h or approximately 151 MEv. Sample P1 was exposed to muons at Pos 3 with two different aperture slit sizes (14 and 48 mm), resulting in a cumulative exposure of 2.25 h or 740 MEv. The depth distribution of stopped muons for each position and the corresponding FWHM (~116 μm), simulated using a Monte Carlo simulation package "musrSim"[14] based on GEANT4,[15] are depicted in Fig. 1(c). Characterization of the muon beam prior to the experiment indicated that the muon beam corresponded well with the aperture slit and extended across a ~14 mm width with a slight Gaussian intensity distribution.

Experiment II intended to distinguish between effects of muon deceleration and implantation. Samples N4 and N5 were exposed to the muon beam simultaneously. N4 was etched in TMAH to a thickness of 270 μm and positioned in front of sample N5 as shown schematically in Fig. 1(d). The samples mounted on the sample holder are shown in Fig. 1(e). Based on simulations, the energy loss upon transmission through sample N4 corresponds to Pos 2. Therefore, the muon implantation into sample N5 is comparable to sample N2, as depicted in Fig. 1(f).
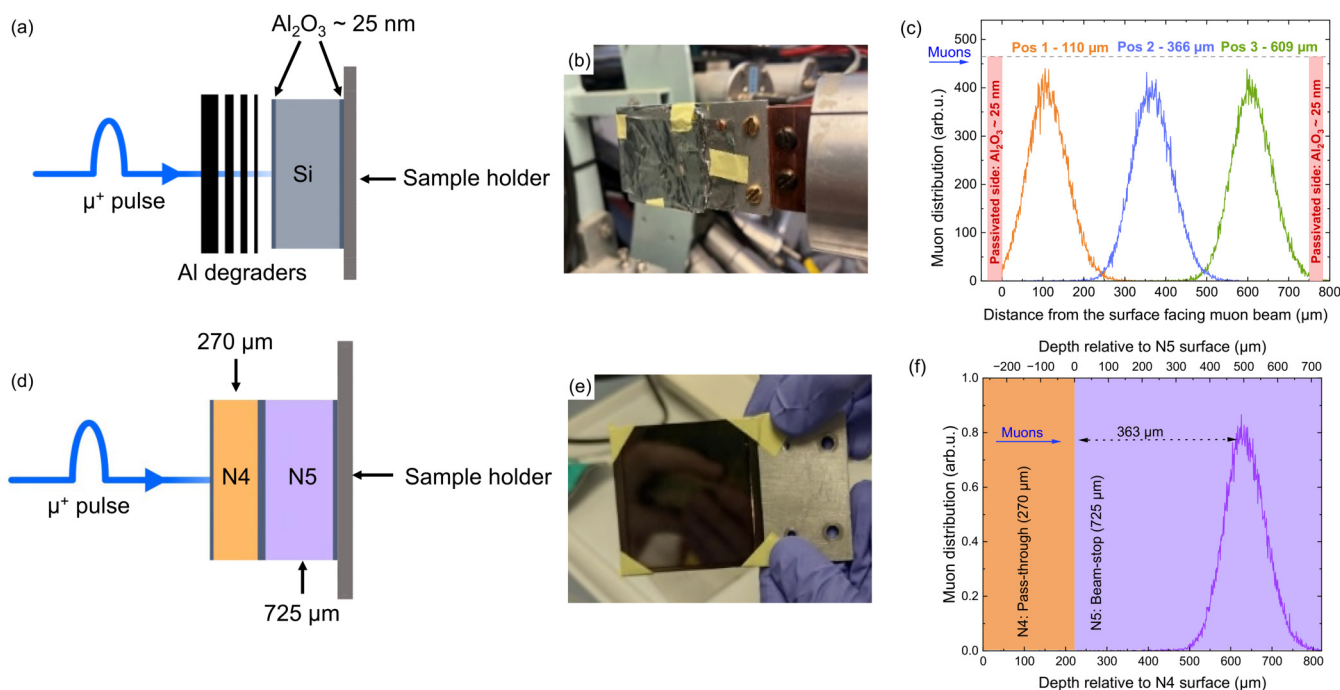
FIG. 1. (a) Schematic representation of muons interacting with silicon for experiment I with different degrader configurations. (b) Photograph of the sample mounted on the closed cycle refrigerator (CCR) with aluminum degraders positioned on the side of muon exposure. (c) Muon distribution profile for various degrader configurations given in Table II, as calculated through Monte Carlo simulations. (d) Schematic representation of muons interacting with silicon for experiment II showing N4 as the pass-through sample and N5 as the beam stop sample with no aluminum degraders used. (e) Photograph of sample N4 ($270\,\mu m$ thick) on top of N5 ($750\,\mu m$ thick) mounted on the sample holder. Both samples measure approximately $5 \times 5\,cm^2$ in size. (f) Muon depth profile in sample N5, as calculated through Monte Carlo simulations.

C. Charge carrier lifetime assessment

Our previous study demonstrated that the defects formed upon muon irradiation have a pronounced effect on effective charge carrier lifetime, τ_{eff}, i.e., introduce recombination of excited electrons and holes in the silicon sample. When assuming the formed defects to be independent point defects, the introduced recombination rate $1/\tau_{eff}$ (ΔR) provides a measure for the density of active defects.[16] In this work, τ_{eff} was assessed via the measurement

TABLE I. Samples used for experiment I and experiment II.

Label	Doping type	Nominal resistivity (Ω cm)	Wafer thickness (μm)	Experiment	Muon beam exposure duration (h)	Estimated total muon dose (MEv)	Muon implantation depth(s) (μm)
P1[a]	p-type	2000	750	I	2.25	740	609
P2	p-type	1000	725	I	12	1476	366
N1	n-type	500–1200	725	I	2.5	151	110, 366, and 609
N2	n-type	500–1200	725	I	12	1430	366
N3	n-type	500–1200	725	I	12	1430	609
N4	n-type	500–1200	270[b]	II	12	1406	Muons pass through
N5	n-type	500–1200	725	II	12	1406	363
N6	n-type	500–1200	725	I	2.5	151	110, 366, and 609

[a]Sample P1 was exposed to muons with slit size of 14 and 48 mm. The estimated muon dose density is cumulative over both exposure conditions.
[b]Sample N4 was etched in TMAH to a thickness of $270\,\mu m$ before deposition of passivation layers. Sample N4 served as a pass-through sample for N5, in which the muons finally stopped.

of conductance or luminescence response upon charge carrier excitation with light.

1. Photoconductance decay

A typical approach for the investigation of charge carrier lifetimes and, hence, silicon material quality is application of transient photoconductance decay (PCD). We apply a Sinton WCT-120PL lifetime tester operating with software version v5.74. In this setup, a flash lamp is used to excite charge carriers in the sample and the decay of the induced excess conductivity is measured inductively using a metal coil as part of an oscillating circuit. The setup used has a coil diameter of 2 cm,[17] hence covering a larger area than was irradiated by the muon beam. Therefore, we consider the values of $\tau_{eff,PCD}$ observed to be semi-quantitative and indicative values only.

2. Photoluminescence imaging

Assessment of the lateral distribution of τ_{eff} is possible through imaging the intensity of photoluminescence (PL)—being the luminescence response arising through radiative recombination of excited charge carriers upon illumination. We used two imaging setups in this work. One setup features a 630 nm LED light source and a Peltier-cooled silicon charge-coupled device (CCD) camera (Apogee Alta F32) to detect the PL signal. By default, this setup images the steady state excess carrier density upon illumination, which is a qualitative measure for effective local charge carrier lifetime. We use consistent LED current settings (corresponding to $\sim$0.01 W cm^{-2} intensity), camera temperature, and integration time between images, which allows for a direct quantitative comparison of signal count rates across each sample and between similar samples.

The second imaging setup used, *modulum*, is described in more detail in Ref. 18. It features 808 nm laser illumination, a Peltier-cooled silicon CCD, a Peltier-cooled sample stage (ensuring sample temperature of 25 °C), and diodes to allow for time-resolved quantitative detection of laser intensity and luminescence response. Through using modulation of illumination intensity, this setup is capable of providing lifetime-calibrated PL images (cPLI).[19,20] Effective lifetimes extracted from *modulum* measurements will be referred to as τ_{eff} in this article. Due to logistical constraints, the use of this setup for sample characterization was limited to after muon exposure (see Sec. II B above) but before any subsequent sample processing. At this stage, each sample was investigated with an image series of 8–9 different intensities between 0.05 and 2 sun equivalents of 808 nm laser illumination. Each sample underwent independent measurements from the front side and the back to assess the potential impact of asymmetric aspects such as muon exposure, sample geometry (polished vs unpolished side), and sample handling (e.g., vacuum grease used to mount samples to the sample holder).

D. Post-muon exposure processing

1. Temporary wet chemical surface passivation

Prior to any experimental procedures, silicone grease from sample mounting was removed using acetone/isopropanol followed

by gentle sonication with a minimal impact anticipated on surface passivation. The Al_2O_3 films were removed with a 1-min immersion in an HF(1%):HCl(1%) solution. Superacid passivation was carried out to temporarily passivate the silicon surface after muon exposure using techniques described in previous works.[21,22] The samples were then sequentially immersed in SC2, TMAH solutions (25%), and SC2 heated at 80 °C for 10 min each. This cleaning procedure is hereafter referred to as SC2-TMAH-SC2. A de-ionized water rinse and a 60 s dip in HF (1%) preceded each cleaning and etching step. Finally, the samples were immersed in HF(1%):HCl (1%) for 5 min to terminate the surface with hydrogen.[11] The superacid solution was prepared in a low humidity (<25%), nitrogen-purged glovebox by dissolving bis(trifluoromethane)sulfonamide (TFSA) in anhydrous pentane at a ratio of 2 mg ml^{-1}. Each silicon sample was immersed in the superacid solution for approximately 60 s before being removed and allowed to dry. The samples were then taken out of the glovebox for re-characterization using PCD and photoluminescence imaging (PLI).

2. Isochronal annealing

To investigate the stability of the created defects, an isochronal annealing study similar to Refs. 23 and 24 was performed. Starting from 80 °C, and successively increasing in annealing temperature, samples were subjected to a cycle of (i) annealing for 30 min in air in a quartz tube furnace, (ii) thorough wet chemical cleaning, etching (SC1-TMAH-SC2 as described in Sec. II A), and subsequent superacid re-passivation. A de-ionized water rinse and a 60 s dip in HF (1%) preceded each cleaning and etching step. Finally, the samples were immersed in HF(1%):HCl(1%) for 5 min (unless otherwise stated), followed by superacid passivation as described above. Samples were subsequently characterized with PCD and PLI to determine at what temperature, if any, the muon-induced recombination was deactivated. Control samples for these experiments included unprocessed substrates (not exposed to muons nor previously passivated) and substrates that had been passivated with Al_2O_3 but not exposed to muons. This latter control did not undergo annealing but serves to illustrate reproducibility of superacid passivation quality and to demonstrate that the re-passivation process does not fundamentally affect sample quality or the measurement routine.

III. RESULTS AND DISCUSSION

A. Impact of surface passivation

Our previous study had found that muon-induced degradation occurred in the bulk of the material, rather than being caused by a degradation of surface passivation performance.[5] We reconfirmed this to be true for the changed beamline setup used in this study by using superacid re-passivation, as discussed in Sec. II D, and PL imaging. Figure 2(a) presents PL intensity for each sample prior to exposure, following muon exposure, and following superacid re-passivation. The samples depicted here comprise both experiments I and II. Of these, a subset of samples was investigated with cPLI, with the extracted carrier lifetimes also shown in Fig. 2(a). PLI further verifies that the damage persists as a localized feature in the sample center even after superacid treatment. A set of examples

is shown in Fig. 2(b). Thus, we are confident to report that the main origin of the lifetime reduction is *within* the crystalline silicon samples. The observed variation in PL intensity prior to muon irradiation ($0.5-5 \times 10^3$ counts s^{-1}) for samples N1–N6 is attributed to differences in surface passivation caused by imperfections arising from sample handling during cleaning, ALD deposition, and subsequent annealing. This variability is often observed for samples processed under these conditions[12] and does not compromise the validity of PL intensity characterization for assessing the effects of muon irradiation.

The formation of defects manifests in a reduction of effective minority charge carrier lifetime τ_{eff} compared to measurements prior to irradiation, as collated in Fig. 2. PL images of the irradiated samples show a low-intensity region located in the sample center—coinciding with the muon irradiation spot—implying that region to be damaged. Although the initial τ_{eff} differed between samples due to the impact of local imperfections, we clearly observe a pronounced reduction of τ_{eff} upon muon exposure. This implies that the initial material and processing quality were sufficient to clearly reproduce our earlier work and demonstrate degradation. The symbols in Fig. 2(a) show the charge carrier lifetimes extracted from cPLI via square route harmonic averaging across suitable regions of interest on each sample after muon exposure. Due to experimental constraints, cPLI measurements were only conducted after muon exposure. Hence, we characterized two regions of interest per sample, denoted as "*best spot*" and "*muon spot*." The *best spot* averages across a region larger than 5×5 mm^2 of high PL intensity. It encompasses lifetime limitation impacts of material quality, surface passivation, and handling. The *muon spot* averages across the central region exposed to muon irradiation. To circumvent impacts of lateral carrier diffusion, this region of interest (ROI) was deliberately chosen smaller than the irradiated region (typically $\sim 3 \times 3$ mm^2). The choice of ROI is illustrated in an example in Fig. 3(a). Comparison of $1/\tau_{eff,muon}$ and $1/\tau_{eff,best}$ allows for extraction of the change in recombination introduced by irradiation,

$$\Delta R = \frac{1}{\tau_{eff,muon}} - \frac{1}{\tau_{eff,best}}. \tag{1}$$

When comparing similar samples and assuming recombination to follow the Shockley–Read–Hall mechanism, this quantity resembles an effective defect concentration, as discussed, e.g., in Ref. 16. The used approach requires the effective lifetimes to be determined at the same charge carrier density Δn. Since the cPLI image stacks do not provide continuous $\tau_{eff}(\Delta n)$ curves, a linear interpolation between neighboring values was used to extract τ_{eff} values at $\Delta n = 1 \times 10^{15}$ cm^{-3}. The samples were measured from the front and the back to test for pronounced asymmetry, which could, for example, be caused by more pronounced damage of one sample surface during handling (e.g., application or removal of vacuum grease) or very surface-near formation of defects. This was not observed, and thus, the multiple measurements per sample instead give an impression of reproducibility.

B. Impact of doping polarity

We first consider experiment I. Samples N2 and P2 were processed identically and subjected to similar doses of muon irradiation for a direct comparison of muon damage. The charge carrier lifetime measured in un-irradiated parts of sample N2 (assessed via $\tau_{eff,best}$) was lower than that observed on P2. This may well be related to more pronounced handling damage combined with a stronger impact of lateral carrier transport paths parallel to the surface of the wafer due to the inversion layer formed in *n*-type substrates when using Al$_2$O$_3$ passivation.[25] This disproportionate impact *could* affect a direct comparison of $\tau_{eff,muon}$ between the samples for cases of small degradation and would lead to an underestimation of damage on *n*-type samples. However, we found that τ_{eff} reduced drastically upon muon exposure, as shown in Fig. 3(b), rendering the lateral transport negligible in comparison. The impact of surface recombination is mostly corrected for using Eq. (1) since it should have a similar effect on both measurements and, hence, cancel out. The resulting values for ΔR for N2 and P2 can be found later in Sec. III D (Fig. 5).

We observe stronger degradation on the *n*-type substrate, corresponding to $\sim 50\%$ more additional recombination. Recombination via point defects or small localized defects can usually be described as linear independent events arising from the product of defect concentration and the individual recombination activity of the defect. This implies two hypotheses for the observed behavior: (a) exposure to similar muon doses introduces more defects in *n*-type silicon than in *p*-type silicon or (b) the defects are more recombination-active. First considering (a), different defect concentrations may arise if the defect(s) in question can heal out at room temperature, and there is an impact of Fermi level position on the enthalpy of this process. Recombination activity being different as per hypothesis (b) is a common consequence of defects being charged since this introduces a favorable interaction with one charge carrier type, e.g., Ref. 26. However, we assess the charge carrier lifetime at excess carrier densities Δn around 10^{15} cm^{-3} and, hence, orders of magnitude above the doping concentration of the wafers. Therefore, the electron and hole densities should be near identical, rendering hypothesis (b) less plausible and implying a concentration difference.

C. Impact of muon transmission vs muon implantation

Samples N4 and N5 were used in experiment II to distinguish between the effects of muon deceleration and implantation. N4 and N5 came from the same original wafer stock, but prior to passivation, sample N4 was thinned down to 270 μm by TMAH etching. The two samples were placed into the muon beam at the same time, with N4 placed in front of N5. This ensured that most muons passed through N4, depositing about 1/3 of their kinetic energy according to the Monte Carlo simulations, and were then stopped in N5 at a depth comparable to Pos 2 (*cf.*, Table II).

Figure 4(a) shows a comparison of PLI measurements before and after muon exposure. We observe a distinct damaged region manifested by low PL intensity in the center of both samples after muon exposure. The width of this dark region (~ 2 cm) is greater than the width of the muon beam (1.4 cm) due to lateral carrier
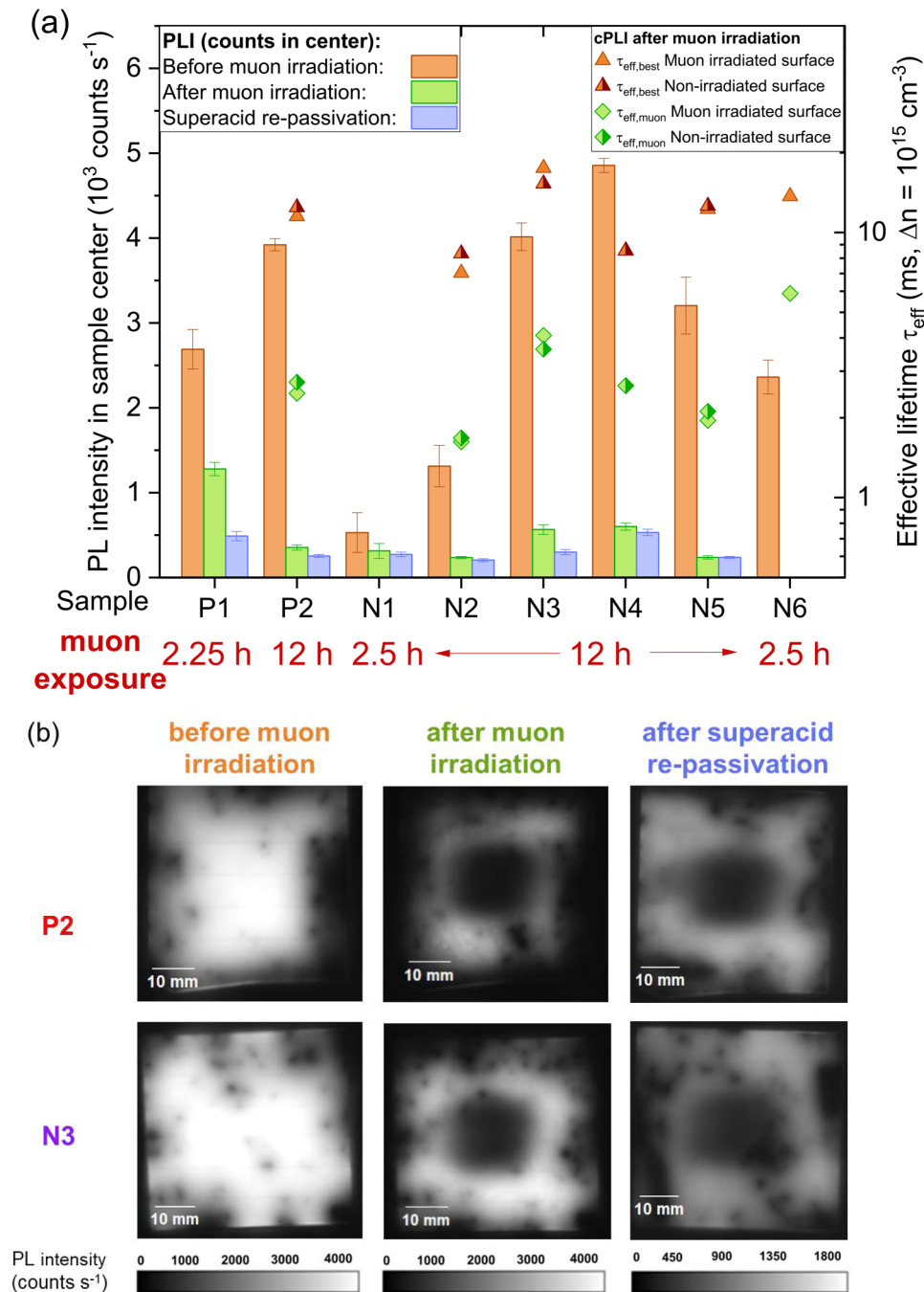
10 August 2024 11:53:52

FIG. 2. (a) Mean PL intensity in sample center (bars) and effective carrier lifetimes τ_{eff} extracted at Δn of 10^{15} cm^{-3} from cPLI measurements. The PL images were recorded at different stages: prior to muon exposure (orange), after muon exposure (green), and following superacid re-passivation (blue). The error bars correspond to the standard deviation of PL counts across the ROI. cPLI measurements were recorded after muon exposure and lifetimes were extracted in a non-exposed region ($\tau_{eff,best}$) and in the sample center ($\tau_{eff,muon}$). (b) Comparison of PL images for p-type sample P2 and n-type sample N3 at different stages to demonstrate that the localized limitation after muon exposure remains upon re-passivation.

diffusion. The damaged region is visible in both N4 and N5, confirming that even transmitted muons create defects in silicon. Note that the absolute emitted PL signal cannot directly be compared between the samples due to their different thicknesses.

Evaluation of $\tau_{eff,muon}$ and $\tau_{eff,best}$ from cPLI measurements is shown in Fig. 4(b) and reveals that sample N5 suffered more damage than sample N4. This seems intuitive at first given that our numerical simulations of muon implantation showed that about
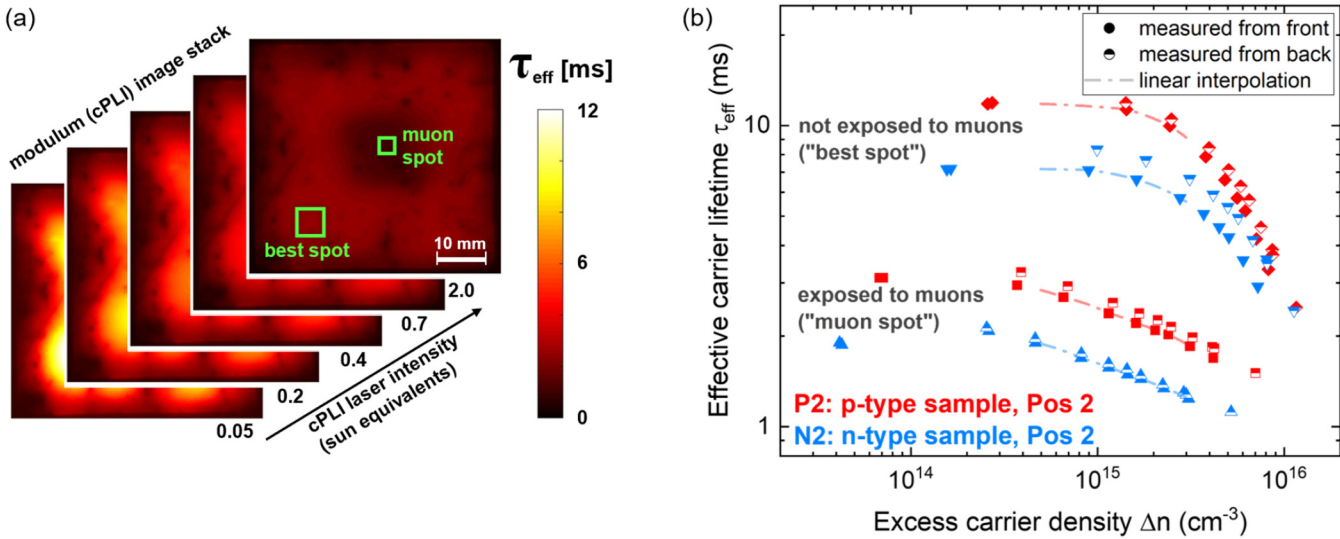
FIG. 3. (a) Illustration of a stack of lifetime-calibrated PL images (cPLI) of a sample (N5) taken after muon exposure and the ROI evaluated for the "*best spot*" and "*muon spot*" evaluated on this sample. (b) Extracted charge carrier lifetimes τ_{eff} of samples P2 and N2, serving to illustrate the different effect of similar muon exposure to silicon of different doping types. The dashed line between points is a linear interpolation.

twice as much kinetic energy was dissipated in it per muon [cf., the area under the respective curves in Fig. 5(a)]. However, sample N4 has been thinned down significantly (to about a third of initial thickness), and thus, more kinetic energy was dissipated per sample volume. The remaining $\tau_{eff,muon}$ level of both samples still supports diffusion lengths far exceeding the sample thickness. Therefore, charge carriers across the sample depth will be impacted by defects even for the asymmetric profile expected for sample N5 [cf., Figs. 1(f) and 5(a)], and the extracted lifetime represents an averaged volume information on crystal damage. This is further supported by only small differences between cPLI measurements performed from the front or back of the samples—especially considering that the surfaces featured different roughness and that the polished side was exposed to vacuum grease.

D. Impact of total dissipated energy

Intuitively, the damage caused to the silicon crystal by muon implantation should scale with the number of implanted muons

and the dissipated energy per particle. As discussed above, Eq. (1) isolates recombination caused by muon implantation. This quantity (ΔR) is affected by several sources of uncertainty and could not be determined for all irradiated samples due to experimental constraints. The extracted ΔR values for all suitable samples are shown in Fig. 5(b) as a function of the product of muon dose ϕ_{muon} and the respective dissipated energy per muon $\Delta E_{kin,muon}$ as determined from the integral of the energy dissipation curves shown in Fig. 5(a). In addition to the difference between p- and n-type materials discussed above, we find the anticipated correlation of damage and dissipated dose. This overall correlation was less pronounced when regarding just ϕ_{muon} or $\Delta E_{kin,muon}$ individually.

An interesting observation concerns the "*pass-through*" sample N4, which is the only sample with a different sample thickness for which ΔR was determined. When plotted against the absolute dissipated energy [Fig. 5(b), gray circle], the sample follows the trend of other n-type samples, as illustrated by the blue shaded region in Fig. 5(b). When plotted against the energy dissipated per volume [i.e., normalized to thickness, orange circle in Fig. 5(a)], the

TABLE II. Degrader configurations used for experiments I and II with muon peak depth into the sample and muon energies at the sample surface calculated by Monte Carlo simulation.

Position	Samples in this configuration	Total aluminum degrader thickness (μm)	Muon implantation peak depth (μm)	Kinetic energy of muons at sample surface (MeV)
Pos 1	N1, N6	484	110	1.43
Pos 2	N1, P2, N2, N6	248	366	2.66
Pos 3	P1, N1, N3, N6	24	609	3.83
"Beam-stop"	N5	[a]	363	2.65

[a]Sample N5 was exposed through 270 μm silicon (sample N4), which corresponds well with the depth of Pos 2 achieved using Al degraders.
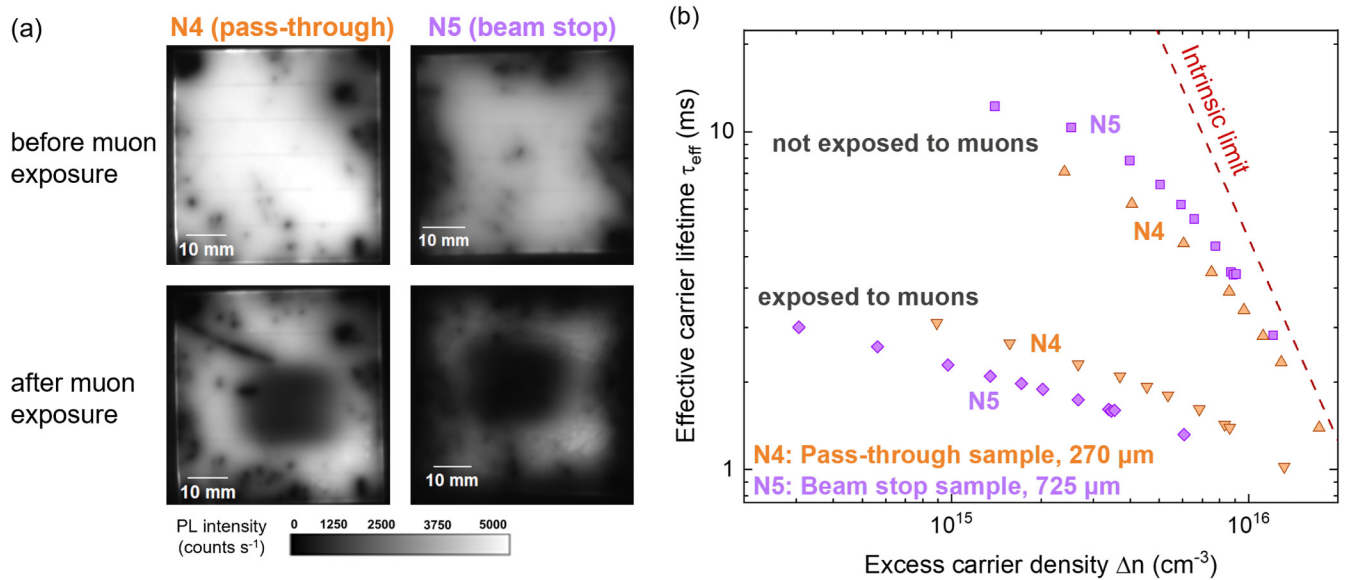
FIG. 4. (a) PL images of samples N4 (left) and N5 (right) with Al_2O_3 surface passivation, prior to (top) and following (bottom) muon exposure. The muon beam passed through N4 and stopped in N5, and both samples show a region of reduced intensity consistent with the beam dimensions in the sample center following muon exposure. The faint grid pattern in the PL images is a PL measurement artifact. (b) Effective lifetime curves extracted from calibrated PL imaging for samples N4 and N5.
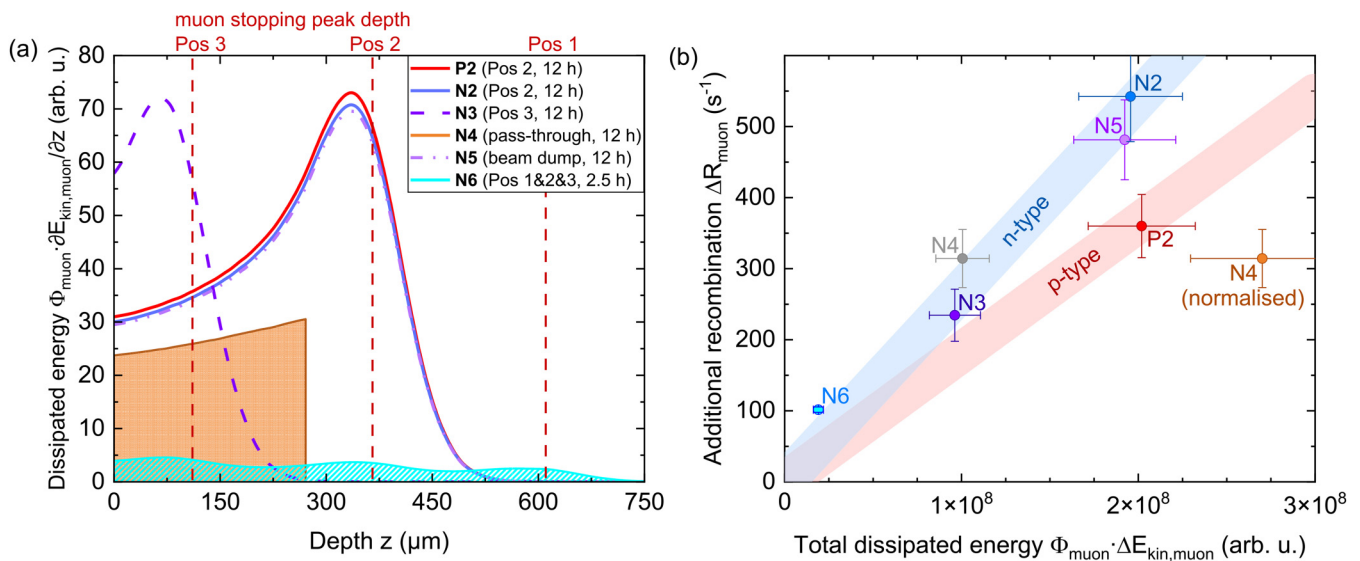

FIG. 5. (a) Depiction of energy dissipation across sample depth. The distribution is shown as the product of muon dose (see Table I) and a GEANT4-based[15] Monte Carlo simulation of muon implantation. Shaded areas serve to illustrate the estimation of total dissipated energy on the examples of samples N4 and N6. (b) Muon-induced damage (observed as additional recombination ΔR) in dependence of the total dissipated energy. The error bars indicate the deviation between repeated determination of ΔR in the y-direction and the uncertainty of ϕ_{muon} and $\Delta E_{kin,muon}$ in the x-direction. The shaded regions serve as guide to the eyes to illustrate a general trend and the discussed difference by doping type. Sample N4 is shown with the total dissipated energy (gray) and with that energy normalized to its smaller sample thickness (orange).

10 August 2024 11:53:52

sample apparently suffered "*too little*" damage. The remaining charge carrier diffusion length in the degraded state is sufficiently long that cPLI τ_{eff} measurements can detect a depth-averaged recombination activity. This is also supported by the similarity of τ_{eff} measured from front or back side of the samples (cf., Fig. 3), the variation of which is indicated with the vertical uncertainty bars in Fig. 5(b). Thus, we regard ΔR as a depth-averaged quantity that should be independent of the actual damage depth profile and, hence, expected the opposite behavior of sample N4. Besides the sample thickness, the main difference to the other *n*-type samples is N4 being the "*pass-through*" sample—muons did not stop in the sample.

Our considerations lead to three hypotheses for this observed discrepancy: (I) additional/more severe damage is caused by slow or stopped muons, (II) damage is caused by the subsequent muon decay, or (III) damage is caused by the resulting emitted positrons. Regarding (I), it is worth noting the twofold increase in energy dissipation shortly before stopping. This is related to increasing interaction of the incoming muon with electrons and bulk atoms, and it would make sense that these interactions would cause additional or other defects. Hypothesis (II) is unlikely since muon decay is not typically impacted by the electromagnetic environment, and hence, no energy dissipation to the silicon lattice is expected. The positrons emitted upon anti-muon decay could give rise to further crystal damage, making hypothesis (III) more plausible. However, since the majority of positrons are emitted at several MeV,[9] they interact weakly with silicon. Furthermore, a share of the positron emission goes back through sample N4 due to the preferential emission along the muon polarization direction,[9] which in the given experiment is opposing the direction of implantation. Thus, we would expect damage arising from muon decay to also occur in sample N4, resulting in more similar overall damage. An aspect that may support hypotheses (II) and (III) is sample N3, which accumulated about half as much ΔR as observed for N5 and N2. Given that muons deposited to Pos 3 decay close to the surface, it would be plausible to expect half as many defects compared to the Pos 2 profile. However, the Pos 3 profile also dissipated about half as much kinetic energy compared to the Pos 2 profile; hence, the effects cannot be distinguished. A sample with extended muon exposure to profile Pos 1 would be useful but is not available. Placing a sample behind subsequently thick degrader foil to fully stop the muons directly before the sample is another option and might be part of future experiments. Less unique information can be extracted from sample N6, which was exposed to low doses of all three profiles. Since two-thirds of the muons were deposited close to one surface, hypotheses (b) and (c) would imply that the sample should accumulate less damage.

E. Defect thermal stability

To investigate the muon-induced defects and their thermal stability, an isochronal annealing study was performed on *n*-type sample N2 and *p*-type sample P1, which were exposed to the muon beam for 12 and 2.25 h, respectively. This section will discuss the investigation into the former. This isochronal annealing experiment involved cycles of annealing at sequentially higher temperatures, interspersed with superacid re-passivation, with the aim of determining whether there was a processing temperature at which the

effects of the muon-induced defects were no longer observed. As the samples in this experiment were both passivated and exposed to muons, a separate control sample was selected, which had been neither exposed to muons nor passivated (denoted "untreated"), in an attempt to separate these two factors. The untreated substrate served to demonstrate the reproducibility of passivation quality and ascertain the impact of repeated re-passivation on sample quality. PL images taken after annealing at selected temperatures are shown in Fig. 6(a). Superacid passivation quality can be variable, as it is strongly affected by underlying substrate surface quality.[22] Indeed, the PL image for the "untreated" sample at 250 °C demonstrates non-uniformity of the passivation in the form of low PL intensity region, which we attribute to damage induced through sample handling. Nevertheless, superacid re-passivation serves as a useful means to characterize quantitatively the effects of thermal processing on these samples.

We observe a substantial decrease in the size of the low-intensity region on sample N2 from 1.8 cm after processing at 80 °C to 0.6 cm after finishing the annealing series. This indicates a reduction in the recombination arising from muon-induced defects. Due to the aforementioned lateral inhomogeneity in muon-exposed samples, limited conclusions can be drawn from QSSPC; hence, we here use PL to characterize these samples. To determine the relative performance of both good and bad regions, measured PL counts were used—similar to the PL proxy method reported previously.[11,27] Two values are compared: the measured counts in the low-intensity region and the average of measured PL counts in three "good" regions to represent more accurately the relative performance across the entire sample, with both values plotted in Fig. 6(b). The PL counts of the "untreated" sample are extracted from the "good" areas of the samples, rather than those with low PL intensity due to assumed sample handling damage, as this "good" area is considered more representative of the overall sample following re-passivation. Extracting the PL counts in this way allows a more quantitative assessment of the PL images, and we observe a general increase in intensity between the initial superacid treatment and the PL image recorded after the 450 °C step. Similar PL counts were observed between the "untreated" sample and the unaffected regions of sample N2. We observe that the PL intensity extracted from sample regions that were not exposed to muon irradiation are similar to that of a sample that was not exposed to muons (i.e., N2 and "untreated"). Through the isochronal annealing study, we see an increase in measured PL in both the "good" and the "bad" regions. The increase in the "good" regions is likely an experimental artifact caused by lateral carrier diffusion in the sample and photon blurring in the CCD; hence, we will focus on the "bad" regions. The increase in PL counts here combined with the reduction in the width of the dark PL region suggests that the treatment reduced recombination in the muon-exposed samples. Since our findings imply that muon exposure creates defects in the sample bulk material (see Sec. III A), the improvement in PL implies that the introduced defects have been passivated or dissolved.

F. Chemical passivation of the defect(s)

The isochronal annealing series resulted in a considerable shrinking of the lower PL intensity region we associate with
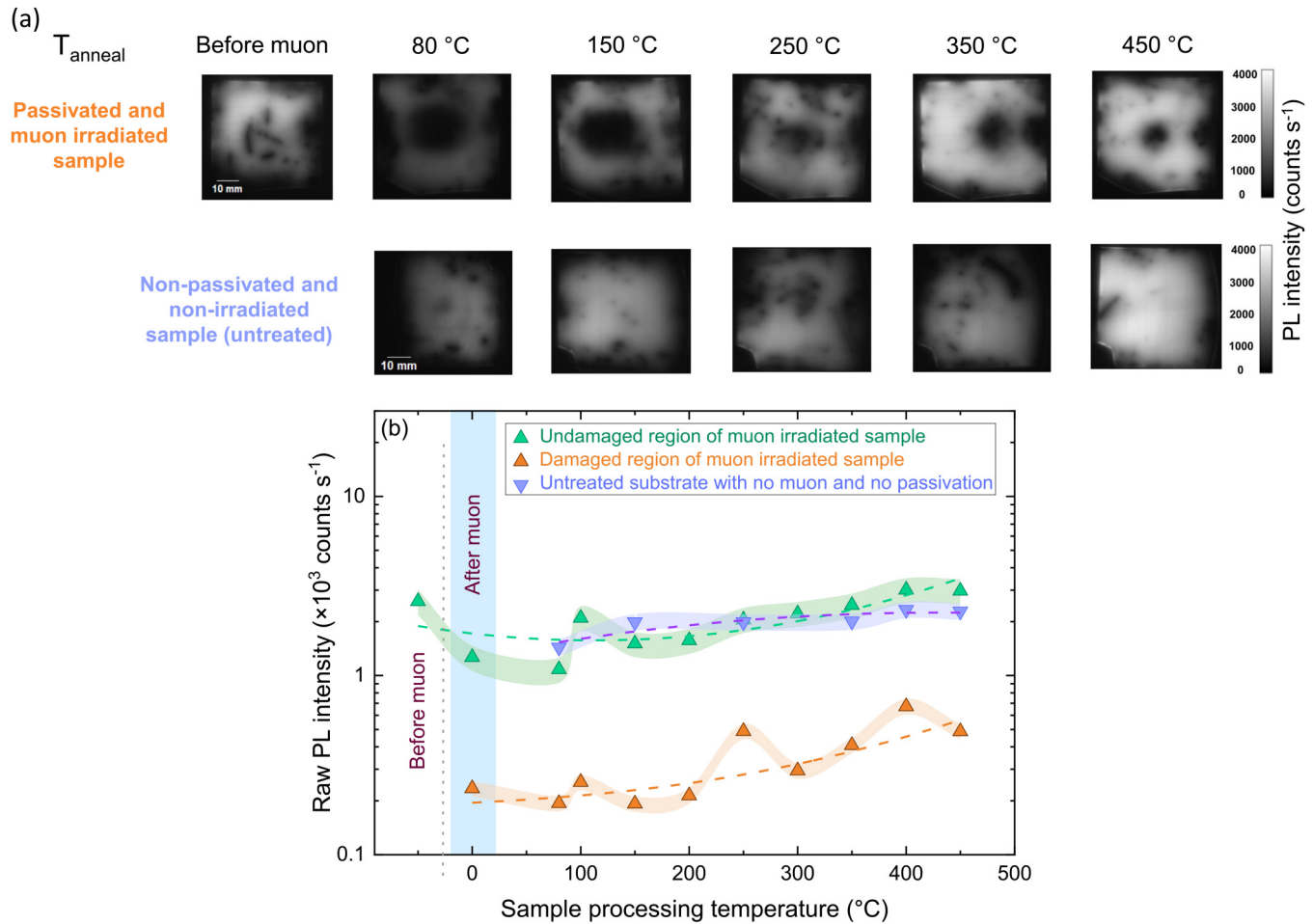
FIG. 6. (a) PL images with superacid passivation taken during the isochronal annealing series for sample N2, which was previously passivated with Al_2O_3 and muon irradiated, and an untreated control sample that had not been previously exposed to muons nor passivated with Al_2O_3. The "before muon" PL image corresponds to sample N2 with the original Al_2O_3 passivation. (b) Mean PL counts, extracted with ImageJ either at a single region in the damaged part of the sample (orange) or averaged across three high intensity regions (green and blue), at each stage of the isochronal annealing experiment. The dashed lines serve as a guide to the eye, and shaded regions correspond to the standard deviation PL of the considered ROI. Samples reach a maximum temperature of $\sim80\,°C$ when being cleaned for superacid passivation; hence, data following first superacid re-passivation experiment (before any annealing) appear at this value on the horizontal axis. Note that, for logistical reasons, the final stage of the cleaning process for the untreated substrate at the $450\,°C$ time point was 2% HF, rather than 1% HF/1% HCl.

muon-induced damage, as shown in Fig. 6(a). However, a small ($\varnothing\sim0.6\,cm$) region of low PL intensity remains visible after annealing at $450\,°C$. To determine whether further processing could reduce the impact of this defect further, sample N2 was cleaned and passivated with $\sim20\,nm$ of Al_2O_3 (as described in Sec. II A). Al_2O_3 films are known to release hydrogen upon annealing, which can electrically passivate defects.[28] Indeed, we observe a significant increase in PL intensity of the muon-exposed region, as illustrated by PL images in Fig. 7(a). Figure 7 also presents effective charge carrier lifetime (extracted at $\Delta n = 1\times10^{15}\,cm^{-3}$) measured via PCD after each process stage. As discussed above this measurement is susceptible to sample inhomogeneity, but the result still demonstrates that the sample features a similar lifetime level as it

did prior to muon exposure. Sample N2 has previously undergone the isochronal annealing series including $450\,°C$ annealing without such full recovery (see Sec. III E). Therefore, we suggest that the most likely mechanism for this observed effect is the passivation of defects by hydrogen.

To investigate this further, we subjected another muon-exposed sample (N3) to Al_2O_3 re-passivation and subsequent 30 min annealing at $450\,°C$, without an interposed isochronal annealing process as shown in Fig. 7(b). Sample N3 had been exposed to muons for a similar duration to N2, but the muons were implanted less deep into the material (Pos 3 vs Pos 2, see Table I). After re-passivation with ALD-deposited Al_2O_3, PL images of this sample showed no evidence of a low PL intensity
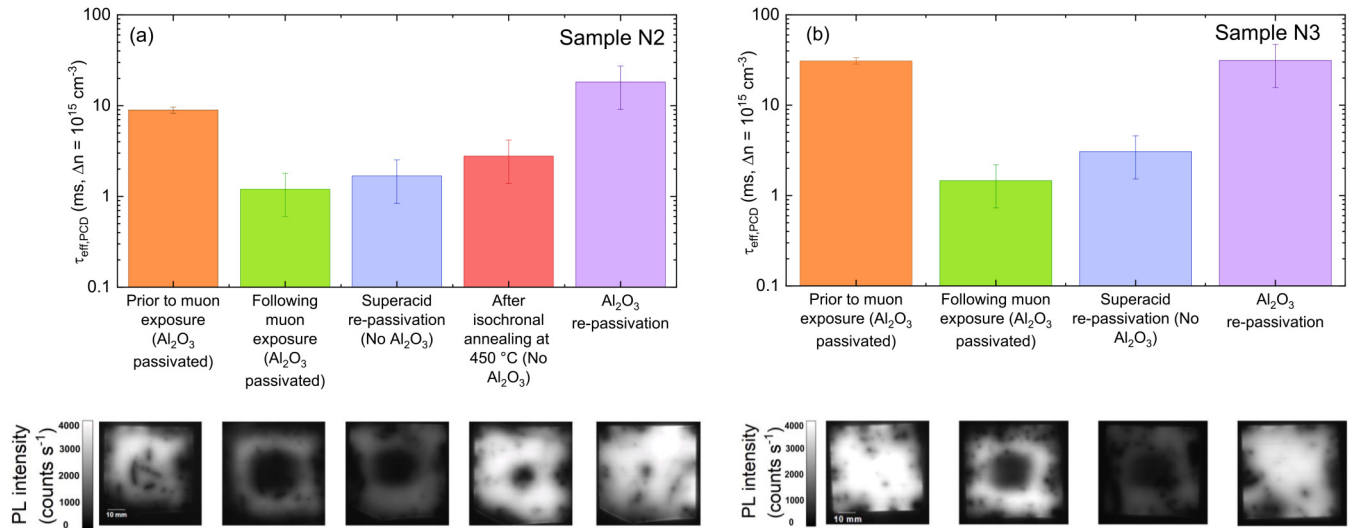
FIG. 7. Top: Effective lifetimes (extracted at $\Delta n = 1 \times 10^{15}$ cm^{-3}) for samples (a) N2 and (b) N3, prior to muon exposure (orange), after muon exposure (green), post-superacid re-passivation (blue), post-isochronal annealing at 450 °C (red), and post-Al$_2$O$_3$ re-passivation (purple). Note that N3 did not go through an isochronal annealing process; hence, there is no red data bar in this case. Extracted effective lifetime data are the average of five measurements. The error bars for "prior to muon" effective lifetime correspond to 8% of the measured value,[29] while that of the others are larger to address the considerable sample inhomogeneity induced on muon exposure. Bottom: Corresponding PL images for samples (a) N2 and (b) N3 at each processing stage.

region related to muon-induced damage. As N3 did not undergo isochronal annealing, this suggests that the impact of Al$_2$O$_3$-related hydrogenation on the deactivation of muon-induced defects exceeds the impact of thermal annealing alone.

IV. CONCLUSIONS

We have demonstrated that exposure to MeV range anti-muons (or positive muons) creates defects in silicon wafers. We analyze both the induced damage and impact of resultant processing. A temporary superacid-based technique was used to clarify that the observed carrier lifetime degradation was indeed caused by bulk defects and not related to the dielectric Al$_2$O$_3$ surface passivation. Our investigation indicates that the muon-induced damage may affect *p*-type substrates more even when subjected to a similar muon dose. There are indications of more defects being present in the *p*-type sample, but our study was not broad enough to decide this. An experiment where muons passed through a thinned sample and were stopped in another demonstrated that defects were created in both samples. A comparison of accumulated damage (assessed via carrier lifetime) found that there is an overall correlation of damage with muon dose and/or dissipated kinetic energy. Hypotheses were formulated to explain this damage in terms of energy dissipated in the lattice or damage being caused by positrons emitted upon muon decay. With the given experiments, we cannot decide with certainty which process is most likely but suggest that the dissipation of the muons' kinetic energy via, e.g., impact ionization and electron scattering[1] is the dominating process for kinetic energies in the MeV range. The formation of defects upon muon exposure and the resulting recombination may affect the functionality of semiconductor devices. This should be kept in mind when utilizing muon spin spectroscopy as a characterization method for semiconductor materials, particularly for materials with high carrier lifetimes. In principle, the damage caused can be monitored *in situ* via photo-μSR, as demonstrated in our earlier work.[5] The muon doses that occurred in this experiment exceed the dose of cosmic muon exposure of devices operated on earth (ca. 60 muons cm^{-2} h^{-1},[30] corresponding to ~13 MEv cm^{-2} across 25-year device lifetime). Given the higher kinetic energy of cosmic muons in the GeV range, we assume that much less interaction would occur. Thus, it does not seem that defects caused by muons would pose a great risk for, e.g., silicon-based photovoltaics.

A thermal annealing study demonstrated a significant reduction in recombination from the muon-induced defects. However, despite annealing at 450 °C, low PL intensity residual remained. The subsequent Al$_2$O$_3$ passivation significantly increased the PL intensity, indicating effective defect passivation. Thus, we propose that the primary mechanism responsible for this is hydrogen passivating the defects. We further validated this by re-passivating a muon-exposed sample that had never undergone thermal annealing and observed no low PL intensity region after Al$_2$O$_3$ passivation. Hence, the Al$_2$O$_3$ re-passivation shows promise in mitigating the muon-induced defects in silicon.

AUTHOR DECLARATIONS

Conflict of Interest

The authors have no conflicts to disclose.

Author Contributions

Anup Yadav and Tim Niewelt contributed equally to this work.

Anup Yadav: Conceptualization (supporting); Data curation (equal); Investigation (lead); Methodology (equal); Visualization (equal); Writing – original draft (lead). **Tim Niewelt:** Conceptualization (lead); Data curation (equal); Investigation (lead); Methodology (equal); Visualization (equal); Writing – original draft (lead). **Sophie L. Pain:** Conceptualization (supporting); Investigation (lead); Methodology (supporting); Visualization (supporting); Writing – original draft (supporting). **Nicholas E. Grant:** Conceptualization (supporting); Methodology (supporting); Supervision (supporting); Writing – review & editing (supporting). **James S. Lord:** Investigation (supporting); Methodology (supporting); Writing – review & editing (supporting). **Koji Yokoyama:** Conceptualization (supporting); Funding acquisition (supporting); Investigation (supporting); Methodology (supporting); Project administration (supporting); Resources (equal); Supervision (supporting); Writing – review & editing (supporting). **John D. Murphy:** Conceptualization (supporting); Funding acquisition (lead); Methodology (supporting); Project administration (lead); Resources (equal); Supervision (lead); Writing – review & editing (lead).

DATA AVAILABILITY

The data that support the findings of this study are openly available in ISIS Neutron and Muon Source Data Catalogue, Ref. 13. Data underpinning the figures can be accessed at https://wrap.warwick.ac.uk/187062/

REFERENCES

[1]S. J. Blundell, R. De Renzi, T. Lancaster, and F. L. Pratt, *Muon Spectroscopy: An Introduction* (Oxford University Press, 2022).
[2]K. Yokoyama, J. Lord, J. Miao, P. Murahari, and A. Drew, Phys. Rev. Lett. **119**, 226601 (2017).
[3]K. Yokoyama, J. Lord, P. Mengyan, M. Goeks, and R. Lichti, Appl. Phys. Lett. **115**, 112101 (2019).
[4]K. Yokoyama, J. Lord, J. Miao, P. Murahari, and A. Drew, Appl. Phys. Lett. **118**, 252105 (2021).
[5]J. D. Murphy, N. E. Grant, S. L. Pain, T. Niewelt, A. Wratten, E. Khorani, V. P. Markevich, A. R. Peaker, P. P. Altermatt, J. S. Lord, and K. Yokoyama, J. Appl. Phys. **132**, 065704 (2022).
[6]S. Cox, Rep. Prog. Phys. **72**, 116501 (2009).
[7]R. Kadono, A. Matsushita, R. M. Macrae, K. Nishiyama, and K. Nagamine, Phys. Rev. Lett. **73**, 2724 (1994).
[8]R. Kiefl and T. Estle, *Semiconductors and Semimetals* (Elsevier, 1991), Vol. 34, p. 547.
[9]B. D. Patterson, Rev. Mod. Phys. **60**, 69 (1988).
[10]T. Lüder, G. Hahn, and B. Terheiden, Energy Proc. **8**, 660 (2011).
[11]N. E. Grant, A. I. Pointon, R. Jefferies, D. Hiller, Y. Han, R. Beanland, M. Walker, and J. D. Murphy, Nanoscale **12**, 17332 (2020).
[12]N. E. Grant, S. L. Pain, E. Khorani, R. Jefferies, A. Wratten, S. McNab, D. Walker, Y. Han, R. Beanland, R. S. Bonilla, and J. D. Murphy, Appl. Surf. Sci. **645**, 158786 (2024).
[13]J. D. Murphy, S. L. Pain, A. Yadav, A. Wratten, K. Yokoyama, T. Niewelt, N. E. Grant, and J. S. Lord, "Passivation of silicon for solar cells and the role of hydrogen," STFC ISIS Neutron and Muon Source (2023).
[14]K. Sedlak, R. Scheuermann, T. Shiroka, A. Stoykov, A. Raselli, and A. Amato, Phys. Proc. **30**, 61 (2012).
[15]S. Agostinelli, J. Allison, K. Amako, J. Apostolakis, H. Araujo, P. Arce, M. Asai, D. Axen, S. Banerjee, G. Barrand, F. Behner, L. Bellagamba, J. Boudreau, L. Broglia, A. Brunengo, H. Burkhardt, S. Chauvie, J. Chuma, R. Chytracek, G. Cooperman, G. Cosmo, P. Degtyarenko, A. Dell'Acqua, G. Depaola, D. Dietrich, R. Enami, A. Feliciello, C. Ferguson, H. Fesefeldt, G. Folger, F. Foppiano, A. Forti, S. Garelli, S. Giani, R. Giannitrapani, D. Gibin, J. J. Gómez Cadenas, I. González, G. Gracia Abril, G. Greeniaus, W. Greiner, V. Grichine, A. Grossheim, S. Guatelli, P. Gumplinger, R. Hamatsu, K. Hashimoto, H. Hasui, A. Heikkinen, A. Howard, V. Ivanchenko, A. Johnson, F. W. Jones, J. Kallenbach, N. Kanaya, M. Kawabata, Y. Kawabata, M. Kawaguti, S. Kelner, P. Kent, A. Kimura, T. Kodama, R. Kokoulin, M. Kossov, H. Kurashige, E. Lamanna, T. Lampén, V. Lara, V. Lefebure, F. Lei, M. Liendl, W. Lockman, F. Longo, S. Magni, M. Maire, E. Medernach, K. Minamimoto, P. Mora de Freitas, Y. Morita, K. Murakami, M. Nagamatu, R. Nartallo, P. Nieminen, T. Nishimura, K. Ohtsubo, M. Okamura, S. O'Neale, Y. Oohata, K. Paech, J. Perl, A. Pfeiffer, M. G. Pia, F. Ranjard, A. Rybin, S. Sadilov, E. Di Salvo, G. Santin, T. Sasaki, N. Savvas, Y. Sawada, S. Scherer, S. Sei, V. Sirotenko, D. Smith, N. Starkov, H. Stoecker, J. Sulkimo, M. Takahata, S. Tanaka, E. Tcherniaev, E. Safai Tehrani, M. Tropeano, P. Truscott, H. Uno, L. Urban, P. Urban, M. Verderi, A. Walkden, W. Wander, H. Weber, J. P. Wellisch, T. Wenaus, D. C. Williams, D. Wright, T. Yamada, H. Yoshida, and D. Zschiesche, Nucl. Instrum. Methods Phys. Res. A **506**, 250 (2003).
[16]S. Rein, *Lifetime Spectroscopy: A Method of Defect Characterization in Silicon for Photovoltaic Applications* (Springer Science & Business Media, 2005), Vol. 85.
[17]L. E. Black and D. H. Macdonald, IEEE J. Photovolt. **9**, 1563 (2019).
[18]H. Höffler, F. Schindler, A. Brand, D. Herrmann, R. Eberle, R. Post, A. Kessel, J. Greulich, and M. Schubert, This paper was presented at the *37th European PV Solar Energy Conference and Exhibition* (WIP GmbH, 2020), Vol. 7, p. 11.
[19]J. A. Giesecke, M. C. Schubert, F. Schindler, and W. Warta, IEEE J. Photovolt. **5**, 313 (2014).
[20]T. Trupke, R. Bardos, and M. Abbott, Appl. Phys. Lett. **87**, 184102 (2005).
[21]N. E. Grant, T. Niewelt, N. R. Wilson, E. C. Wheeler-Jones, J. Bullock, M. Al-Amin, M. C. Schubert, A. C. van Veen, A. Javey, and J. D. Murphy, IEEE J. Photovolt. **7**, 1574 (2017).
[22]A. I. Pointon, N. E. Grant, E. C. Wheeler-Jones, P. P. Altermatt, and J. D. Murphy, Sol. Energy Mater. Sol. Cells **183**, 164 (2018).
[23]N. Grant, F. Rougieux, D. Macdonald, J. Bullock, and Y. Wan, J. Appl. Phys. **117**, 055711 (2015).
[24]N. E. Grant, F. E. Rougieux, and D. Macdonald, Solid State Phenom. **242**, 120 (2016).
[25]B. Veith, T. Ohrdes, F. Werner, R. Brendel, P. P. Altermatt, N.-P. Harder, and J. Schmidt, Sol. Energy Mater. Sol. Cells **120**, 436 (2014).
[26]D. Macdonald and L. Geerligs, Appl. Phys. Lett. **85**, 4061 (2004).
[27]T. Trupke, R. Bardos, M. Schubert, and W. Warta, Appl. Phys. Lett. **89**, 044107 (2006).
[28]G. Dingemans, F. Einsele, W. Beyer, M. Van de Sanden, and W. Kessels, J. Appl. Phys. **111**, 093713 (2012).
[29]A. L. Blum, J. S. Swirhun, R. A. Sinton, F. Yan, S. Herasimenka, T. Roth, K. Lauer, J. Haunschild, B. Lim, K. Bothe, Z. Hameiri, B. Seipel, R. Xiong, M. Dhamrin, and J. D. Murphy, IEEE J. Photovolt. **4**, 525 (2013).
[30]J.-L. Autran, D. Munteanu, T. Saad Saoud, and S. Moindjie, Nucl. Instrum. Methods Phys. Res. A **903**, 77 (2018).